RSC Advances

PAPER

View Article Online
View Journal | View Issue

Cite this: *RSC Adv.*, 2025, **15**, 19726

Sustainable production and antibacterial efficacy of silver nanoparticles on cellulose nanofibers from mushroom waste

Charzen Mae Kinoan [ab] and Haliza Katas [*a]

Underutilized agricultural wastes, such as spent mushroom substrate (SMS), present valuable opportunities for developing sustainable biomedical materials. In this study, cellulose nanofibers (CNFs) were successfully isolated from SMS through a chemo-mechanical process, while the water extract of SMS (WESMS) served as a green reducing agent for the simultaneous synthesis and *in situ* loading of silver nanoparticles (AgNPs) onto TEMPO-oxidized CNFs (AgNP/ToCNF). The chemical structure of the isolated cellulose was characterized using ATR-FTIR, while UV-vis spectroscopy confirmed the successful synthesis and AgNPs loading, showing a maximum absorbance at 424 nm. The resulting hybrid nanomaterial exhibited a nanofiber width diameter range of 273.5–318.5 nm, while the AgNPs had an average diameter of 34.04 nm. The antimicrobial efficacy of AgNP/ToCNF was evaluated against *S. aureus*, *P. aeruginosa*, and *E. coli* using agar well diffusion, broth microdilution, time-kill, and cell membrane leakage assays. AgNP/ToCNF exhibited MIC_{90} values of 250 μg mL^{-1} against *S. aureus* and 125 μg mL^{-1} against *P. aeruginosa* and *E. coli*, whereas free-state AgNPs showed MIC_{90} values of 62.5 μg mL^{-1} against *S. aureus* and 31.25 μg mL^{-1} against *P. aeruginosa* and *E. coli*. Both compounds demonstrated bactericidal activity against all three bacterial strains. Cytotoxicity was assessed using the LDH assay, revealing a concentration-dependent toxicity pattern. Notably, AgNP/ToCNF exhibited minimal toxicity to human dermal fibroblasts (HDFs) at concentrations ≤500 μg mL^{-1} after 72 hours, while free-state AgNPs induced >67% cytotoxicity. Although CNFs derived from SMS lacked intrinsic antimicrobial activity, their incorporation with AgNPs significantly enhanced antibacterial efficacy while simultaneously reducing AgNPs-induced cytotoxicity in mammalian cells. These findings underscore the potential of SMS-derived CNFs as biocompatible nanocarriers for AgNPs and other antibacterial agents, offering a sustainable and eco-friendly approach to developing antimicrobial biomaterials. This study explores the feasibility of upcycling SMS into high-value biomedical products, creating opportunities for future applications in wound healing, antimicrobial coatings, and medical nanocomposites.

Received 25th March 2025
Accepted 29th May 2025

DOI: 10.1039/d5ra02087e

rsc.li/rsc-advances

Introduction

The sustainable management of agricultural waste is a growing global concern due to its environmental and economic implications.[1–3] Among various types of biomass waste, spent mushroom substrate (SMS)—a byproduct generated in large quantities during mushroom cultivation that is high in organic matter and low in toxic elements—represents an underutilized resource with high potential for value-added applications.[4,5] Approximately 5 kilograms are generated for every kilogram of mushrooms cultivated, creating a notable challenge in terms of disposal.[6,7] Conventional disposal techniques, such as incineration and landfilling, contribute to environmental degradation through the release of harmful greenhouse gases,[8–10] and the increased risk of public health issues such as respiratory problems.[11] Therefore, the development of sustainable and innovative strategies to repurpose SMS is both timely and necessary.

SMS is predominantly composed of lignocellulosic biomass, such as cellulose, which accounts for 25–47% of its dry weight.[12–18] Cellulose and its derivatives have been extensively studied as bio-based materials for tissue engineering and drug delivery due to their biocompatibility, functionality, flexibility, and mechanical strength.[19–21] Recent advances in nanotechnology have enabled the extraction of nanocellulose—a biodegradable nanomaterial with enhanced surface area, mechanical performance, and functionality—from various lignocellulosic masses. Nanocellulose has demonstrated significant potential in fields such as food packaging, pharmaceuticals, and

[a]*Centre for Drug Delivery Technology and Vaccine (CENTRIC), Faculty of Pharmacy, Universiti Kebangsaan Malaysia, Jalan Raja Muda Abdul Aziz, Kuala Lumpur, 50300, Malaysia. E-mail: haliza.katas@ukm.edu.my; Fax: +60-3-26983271; Tel: +60-3-9289797*

[b]*Department of Pharmacy, College of Pharmacy and Medical Technology, University of San Agustin, Iloilo City, Philippines*

regenerative medicine.[22–25] However, its application in wound healing remains limited due to the absence of inherent antimicrobial properties.[26–28] One promising strategy to overcome this limitation involves the functionalization of nanocellulose with antimicrobial metal nanoparticles, such as zinc, gold, and silver. This approach not imparts antimicrobial properties to the nanomaterial but also controls the release of the metal ions and reduces their cytotoxicity.[29]

SMS is not only an abundant source of nanocellulose but its water extract has also been studied as a reducing agent for metal nanoparticles.[30] LC-MS analysis of the water extract of SMS (WESMS) reveals the presence of abundant fatty acid derivatives, such as vanillic and decanoic acid – compounds useful for synthesizing metal nanoparticles.[30–32] This positions SMS as a promising starting material for developing nanomaterials applicable in various scientific fields.

Based on our current understanding, the integrated use of SMS both as a source of cellulose nanofibers (CNF) and as a green reducing agent for *in situ* synthesis of silver nanoparticles (AgNPs) has not been explored. In this study, we present a novel and sustainable method for producing AgNP-loaded TEMPO-oxidized cellulose nanofibers (AgNP/ToCNF) from SMS. The antibacterial activity of AgNP/ToCNF was investigated using agar well diffusion, microbroth dilution assay, time-kill kinetics, and cell membrane leakage assay. Furthermore, cell proliferation and nanomaterial cytotoxicity were also assessed using lactate dehydrogenase (LDH) and Alamar Blue assays. This dual-functional approach to utilizing SMS not only contributes to waste valorization but also offers a potential platform for developing low-cost, biodegradable, and antimicrobial biomaterials for medical applications.

Experimental section

Materials

Spent mushroom substrate (SMS) of *Pleurotus ostreatus* (oyster mushroom) was kindly provided by Nas Agro Farm, Sepang, Malaysia. Silver nitrate ($AgNO_3$) (ACS reagent grade) and low molecular weight (LMW) chitosan (50–190 kDa, 75–85% deacetylated) were purchased from Sigma-Aldrich, MO, USA. Sodium hydroxide (NaOH) and 10% sodium hypochlorite (NaOCl), used in the isolation of cellulose nanofibers, were obtained from Bio3 Scientific Sdn. Bhd., Puchong, Malaysia. 2,2,6,6-Tetramethylpiperidine-1-oxyl (TEMPO) and sodium bromide (NaBr), used for TEMPO-mediated oxidation, were acquired from Sigma-Aldrich, MO, USA, and Bio3 Scientific Sdn. Bhd., Puchong, Malaysia, respectively.

Three bacterial strains—*Staphylococcus aureus* ATCC 25923, *Pseudomonas aeruginosa* ATCC 27853, and *Escherichia coli* ATCC 25927—were obtained from Universiti Kebangsaan Malaysia, Kuala Lumpur, Malaysia. Mueller–Hinton broth (MHB), Mueller–Hinton agar (MHA), and ciprofloxacin hydrochloride were purchased from TargetMol, MA, USA.

Primary human dermal fibroblasts (HDF, passage 0) were purchased from ATCC, VA, USA. Dulbecco's Modified Eagle Medium/Ham's F-12 (DMEM/F-12), supplemented with L-glutamine, sodium pyruvate, and HEPES, as well as trypsin–EDTA solution (2.5 g per L trypsin, 1 mmol per L EDTA), were obtained from Nacalai Tesque, Kyoto, Japan. Fetal bovine serum (FBS) and penicillin–streptomycin solutions were sourced from Tico Europe, Amstelveen, Netherlands. The Alamar Blue cell proliferation reagent was purchased from Invitrogen, MA, USA, and the LDH cytotoxicity assay kit was obtained from Canvax, Valladolid, Spain.

Water extraction of SMS (WESMS)

The starch binder from the SMS was removed, and the fibers were dried at 40 °C for 48 hours. The dried samples were then ground using a Pulverisette 14 grinder equipped with a 1.0 mm sieve ring at 10 000 rpm and stored in a sealed container. Subsequently, 20 g of SMS fibers were soaked in 100 mL of purified water and heated at 60 °C for 30 minutes with continuous stirring. The mixture was filtered using Whatman No. 1 filter paper. The solid residue was retained for CNF isolation (see Subsection: Preparation of SMS Fibers). The resulting filtrate was centrifuged at 5000 rpm, filtered again to completely remove any remaining fibers, and stored at 4 °C until use.

Isolation of CNF from SMS

Preparation of SMS fibers. The residue obtained after water extraction of SMS was oven-dried at 60 °C for 24 hours and then finely ground using a mortar and pestle. The resulting fibers were subsequently subjected to sequential treatments under controlled conditions using standardized protocols to ensure consistency and reproducibility.

Alkaline treatment. SMS fibers were treated with varying concentrations of NaOH (2%, 4%, 8%, 16%, and 32% w/v) at 80 °C for 2 hours. The treated fibers were then washed with distilled water until neutral pH was achieved and subsequently dried in an oven at 60 °C for 24 hours. One gram of each treated sample was reserved for biomass composition analysis using the Chesson–Datta method.

Bleaching. The alkali-pretreated SMS fibers were then bleached with 10% NaOCl at 80 °C for 2 h until decolorization, washed with distilled water to neutral pH, and oven-dried at 60 °C for 24 h. One gram of each bleached sample was reserved for biomass composition analysis using the Chesson–Datta method.

Chesson–Datta biomass composition determination. The lignocellulosic components (lignin, hemicellulose, and cellulose) were quantified using the Chesson–Datta method. One gram (a) of the dried sample was soaked in distilled water at 100 °C for 1 hour. The fibers were then filtered and oven-dried until a constant weight (b) was obtained. The dried residue (b) was suspended in 150 mL of 1 N H_2SO_4 and refluxed in a water bath at 100 °C for 1 hour. The mixture was filtered, and the residue was washed with distilled water to neutrality and then dried to a constant weight (c). Next, 10 mL of 72% H_2SO_4 was added to the residue (c) and allowed to react at room temperature for 4 hours. The sulfuric acid was subsequently diluted to 4%, and the mixture was refluxed in a water bath at 100 °C for 1 hour. The resulting residue was filtered, washed to neutrality,

and dried to a constant weight (d). Finally, the residue was ignited in a muffle furnace at 600 °C for 4 hours or until a constant weight (e) was obtained.

The percentages of lignin, hemicellulose, and cellulose in the biomass were then calculated as follows:

$$\%\text{Extractives} = \frac{b-a}{a} \times 100 \quad (1)$$

$$\%\text{Hemicellulose} = \frac{b-c}{a} \times 100 \quad (2)$$

$$\%\text{Cellulose} = \frac{c-d}{a} \times \ 100 \quad (3)$$

$$\%\text{Lignin} = \frac{d-e}{a} \times 100 \quad (4)$$

$$\%\text{Ash content} = \frac{e}{a} \times 100 \quad (5)$$

TEMPO oxidation. The procedure was adapted from the protocol developed by Isogai *et al.* with minor modifications.[33] First, the bleached fibers were finely ground using a mortar and pestle and then subjected to TEMPO-mediated oxidation. The oxidation solution was prepared by dissolving 0.1 mmol of TEMPO and 1 mmol of NaBr in 100 mL of purified water. The ground fibers were added to the solution at a 1 : 100 (w/v) ratio. Oxidation was initiated by adding 10 mmol of NaOCl per gram of fiber to the suspension at room temperature, under continuous stirring at 500 rpm. The pH was maintained at 10 using 0.5 M NaOH throughout the reaction. After one hour, the oxidation was quenched by adding 30 mL of denatured alcohol. The oxidized cellulose nanofibers were then washed twice with distilled water *via* vacuum filtration. Structural modification was confirmed by ATR-FTIR analysis (PerkinElmer Spectrum 100, Waltham, MA, USA).

Mechanical disintegration. A slurry of TEMPO-oxidized cellulose nanofibers (ToCNFs) in 25 mL water at 0.5% (w/v) was stirred at 1000 rpm for 6 hours prior to ultrasonication for 30 minutes. The resulting suspension was then centrifuged at 5000 rpm to separate large fibers from the nanofibers.

Simultaneous green synthesis and *in situ* loading of AgNPs to ToCNFs

The nanocomposite was prepared following the procedure described by Shin *et al.* and Suleman Ismail Abdalla *et al.* with some modifications.[30,34] Briefly, a slurry of ToCNFs and 0.01 M $AgNO_3$ were mixed in a 1 : 1 ratio and heated at 37 °C for 1 hour. The fibers were then collected and washed to remove unreacted $AgNO_3$. The ToCNFs/Ag^+ were subsequently reacted with SMS water extract in a 1 : 5 ratio until the mixture turned reddish brown—a visual indication of AgNP formation. To confirm the synthesis of AgNPs, the mixture was analyzed by UV-vis spectroscopy (Genesys™, ThermoFisher, Waltham, MA, USA) across a scan range of 200–700 nm. A characteristic absorption peak between 400 and 500 nm confirmed the presence of AgNPs. The mixture was then sonicated for 20 minutes and stirred at room temperature for 30 minutes. It was subjected to ultracentrifugation (15 000 rpm for 15 minutes) to remove unreacted components and washed three times with purified water. The resulting AgNP-loaded ToCNFs were resuspended in 5 mL of deionized water and stored at −80 °C prior to lyophilization. Freeze-drying was performed using a ScanVac Coolsafe (Labogene, Lillerød, DK) at −40 °C to −60 °C for 48 hours until a constant weight was achieved. The morphology of the lyophilized nanocomposite was examined using SEM.

Characterization of ToCNF and AgNP/ToCNF

Zeta potential, size distribution, and morphology. The zeta potentials of ToCNFs and AgNP/ToCNF were measured at 25 °C using Malvern Zetasizer Nano ZS (Malvern Instruments, Worcestershire, UK). Measurements were performed in triplicate, and results are presented as the mean ± standard deviation. The morphology and size distribution of the samples were analyzed by scanning electron microscopy (SEM; Zeiss, Wetzlar, Germany). Prior to analysis, samples were stored at −80 °C for 72 hours and subsequently lyophilized for 48 hours using a freeze dryer.

Evaluation of antibacterial activity

Inoculum preparation by growth medium. *S. aureus* (ATCC 25923), *E. coli* (ATCC 25927), and *P. aeruginosa* (ATCC 27853) were cultured on Mueller–Hinton agar (MHA) plates using the streak method and incubated at 37 °C for 18 hours (Memmert, Büchenbach, Germany). Inocula were prepared by transferring three colonies from each plate into a universal bottle containing 10 mL of Mueller–Hinton broth (MHB) using a sterile loop. The bacterial suspensions were incubated overnight to promote growth. After 18 hours, the turbidity of each culture was adjusted spectrophotometrically to an absorbance of 0.08–0.10 at 625 nm by diluting with sterile broth, resulting in a standardized microbial suspension of approximately 1×10^8 CFU mL^{-1} for all strains.

Agar well diffusion assay. Preliminary screening of the samples against *S. aureus*, *E. coli*, and *P. aeruginosa* was conducted using the agar well diffusion assay. Standardized bacterial suspensions (1×10^8 CFU mL^{-1}) for each strain were prepared and uniformly spread on Mueller–Hinton agar (MHA) plates using an L-shaped cell spreader. Five wells, each 6 mm in diameter, were then created on the agar surface using a sterile pipette tip. Ciprofloxacin HCl (20 μg mL^{-1}) and distilled water served as the positive and negative controls, respectively. Fifty microliters of AgNPs, ToCNFs, and AgNP/ToCNF suspensions at concentrations of 500 and 1000 μg mL^{-1} were added to the wells. The plates were incubated at 37 °C for 18 hours, after which the diameters of the inhibition zones were measured with a vernier caliper. Samples exhibiting inhibition zones larger than 4.0 mm were considered to possess antibacterial activity and were selected for further antibacterial profiling and membrane leakage assays. The experiments were performed in six independent trials.

Microbroth dilution assay. Two-fold serial dilutions of the samples (ranging from 1000 to 2 μg mL^{-1}) were prepared using

Mueller–Hinton broth (MHB) as the diluent. The standardized bacterial suspension was diluted 1 : 100 with MHB to achieve approximately 1×10^6 CFU mL^{-1}. Subsequently, 100 μL of each bacterial strain suspension was added to wells of a 96-well plate containing 100 μL of the treatment samples, resulting in a final bacterial concentration of 5×10^5 CFU mL^{-1}. The plates were then incubated at 37 °C for 18 hours. Bacterial growth was measured by optical density at 600 nm (OD600) using a microplate reader (Multiskan™ FC, ThermoFisher, Waltham, MA, USA). The percentage of growth inhibition was calculated to determine the minimum concentration that inhibits 90% of bacterial growth (MIC_{90}).

Time-kill assay. The procedure used for the time-kill kinetics was adopted from Tenover *et al.*[35] Time-kill kinetics of the three bacterial strains were conducted using Mueller–Hinton broth supplemented with test compounds at their respective MIC, two times MIC, and four times MIC. Growth controls were included in each experiment. Ciprofloxacin HCl (20 μg mL^{-1}) was used as the positive control. The initial inoculum was adjusted to 5×10^5 to 5×10^6 CFU mL^{-1}. Viability counts of cultures containing test compounds were performed at 0, 3, 6, 12, and 24 hours. Colony counts were determined from plates containing 30 to 300 bacterial colonies, with an upper sensitivity limit set at 300 CFU mL^{-1}. Time-kill assays were analyzed to determine which antimicrobial agents produced a $\Delta\log 10$ CFU mL^{-1} reduction of −1 (90% killing), −2 (99% killing), and −3 (99.9% killing). Assay readings at 3, 6, 12, and 24 hours were compared to bacterial counts at 0 hours. Bactericidal activity was defined as the lowest antimicrobial agent concentration that reduced the original inoculum by ≥3 log 10 CFU mL^{-1} (99.9%), while bacteriostatic activity was defined as a reduction of <3 log 10 CFU mL^{-1}. All Petri dishes with no signs of bacterial growth were allowed to incubate for an additional 24 hours to confirm bactericidal activity.

Cell membrane leakage assay. Overnight broth cultures of *S. aureus*, *P. aeruginosa*, and *E. coli* were used in this experiment. The bacterial inocula were then exposed to the test compounds at their respective MIC, two times MIC, and four times MIC for 4 and 8 hours. Briefly, 200 μL of the cell supernatants were transferred to a 96-well plate. Leaked nucleic acids were measured at 260 nm, and protein leakage was measured at 280 nm using a microplate reader. Tween 80 (5%) was used as the positive control.

In vitro proliferative effects and cytotoxicity

Alamar blue cell proliferation assay. Human dermal fibroblast (HDF) cells (1.0×10^4 cells per well) were seeded in a 96-well plate containing 90 μL of DMEM and incubated for 24 hours until approximately 70% confluency was achieved. All cells were maintained in an incubator at 37 °C in a humidified atmosphere of 5% CO_2 and 95% air. After 24 hours, the cells were treated with 10 μL of AgNP, AgNP/ToCNF, and ToCNF at concentrations of 125, 250, 500, 750, and 1000 μg mL^{-1}. Blank media without cells was used as the negative control, while untreated cells in DMEM served as the positive control. The cells were then incubated for 24, 48, and 72 hours. After each incubation period, 10 μL of Alamar Blue reagent (10% of the well volume) was aseptically added to the wells and incubated for a further 3 hours. The absorbance of each sample was measured at 570 and 600 nm using a microplate reader (Biotek PowerWave XS, Marshall Scientific, NH, USA) at 24, 48, and 72 hours. The number of viable cells was calculated as a percentage of Alamar Blue reduction (eqn (6)).

$$\text{AB reduction } \% = \frac{[(\varepsilon_{ox}\lambda 2)(A\lambda 1)] - (\varepsilon_{ox}\lambda 1)(A\lambda 2)}{(\varepsilon_{red}\lambda 1)\left(A'\lambda 2\right) - (\varepsilon_{red}\lambda 2)\left(A'\lambda 1\right)} \times 100 \quad (6)$$

where $\varepsilon\lambda 1$ and $\varepsilon\lambda 2$ are constants representing the molar extinction coefficient of AB at 570 and 600 nm, respectively, in the oxidized (ε_{ox}) and reduced (ε_{red}) forms. The constant values are 117 216 ($\varepsilon_{ox}\lambda 2$), 80 586 ($\varepsilon_{ox}\lambda 1$), 155 677 ($\varepsilon_{red}\lambda 1$), and 14 652 ($\varepsilon_{red}\lambda 2$). $A\lambda 1$ and $A\lambda 2$ represent the absorbance of the test wells at 570 and 600 nm, respectively. $A'\lambda 1$ and $A'\lambda 2$ represent the absorbance of the negative control wells at 570 and 600 nm, respectively. The values of AB reduction % were corrected for background values of negative controls containing medium without cells.

The relative cell proliferation was then calculated to quantify the cell viability effects of the test compounds to HDF. The values obtained from treated and untreated cells were used to compute the relative cell proliferation percentage (%RCP) using the formula below (eqn (7)):

$$\%\text{RCP} = \frac{(\text{AB reduction of treated cells})}{(\text{AB reduction of untreated cells})} \times 100 \quad (7)$$

LDH cytotoxicity assay. HDF cells were prepared and treated as described in 2.8. For each time point, 50 μL of the cell culture supernatant from each well was transferred to a new 96-well plate before 50 μL of the LDH reaction mixture was added. Cells treated with lysis solution of the assay kit representing maximal LDH release were used as the positive control and untreated cells were used as a blank to represent background LDH release. The intensity was then measured using a microplate reader (Thermo Scientific Multiskan GO, Thermo Fisher Scientific, MA, USA) at 450 nm. Relative cytotoxicity (%RCyt) was then calculated (eqn (8)):

$$\%\text{RCyt} = \frac{\text{Abs experimental} - \text{Abs untreated}}{\text{Abs lysis control} - \text{Abs untreated}} \times 100 \quad (8)$$

Statistical analysis

All statistical analyses were performed using GraphPad Prism 10. Data are presented as mean ± standard deviation (SD). For comparisons involving a single independent variable, one-way ANOVA was followed by Tukey's post hoc test. For analyses involving two independent variables, two-way ANOVA were performed followed by Tukey's post hoc test for pairwise comparisons. A p-value of <0.05 was considered statistically significant.

Results and discussion

Isolation of CNF from SMS

Fig. 1 shows the diagram illustrating the isolation of CNF extracted from SMS. SMS fibers underwent alkaline hydrolysis

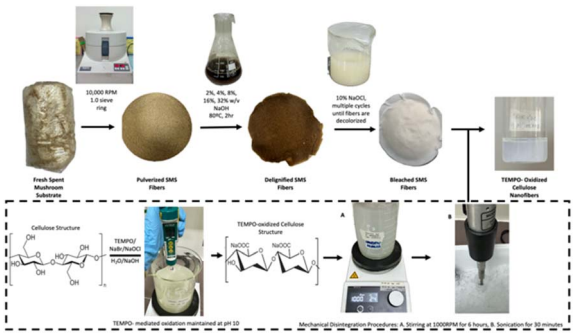

Fig. 1 Schematic diagram of the chemo-mechanical process used to isolate cellulose nanofibers (CNF) from spent mushroom substrate (SMS).

using varying concentrations of NaOH, followed by bleaching with 10% NaOCl to remove lignin—a complex polymer in plant cell walls that can hinder the extraction of cellulose fibers. Different concentrations of NaOH were tested to determine the optimal level for effectively removing lignin from the raw material. Subsequently, the fibers were bleached with 10% NaOCl for 3 cycles to eliminate any remaining lignin and to decolorize the fibers.

As shown in Fig. 2, the highest yield of 43.21% ± 0.73 was obtained using 2% NaOH under bleaching conditions. Increasing the NaOH concentration to 4% and 8% resulted in a gradual decline in yield to 40.24% ± 0.48 and 38.25% ± 0.44, respectively. At even higher concentrations (16% and 32%), the yield further dropped to approximately 32.8%, indicating a significant reduction in CNF recovery. This trend suggests that as the NaOH concentration increases, the CNF yield decreases. Apart from losses incurred during transferring, filtering, and washing, a reduction in weight typically indicates the effective degradation or removal of lignin and other non-cellulosic components from the biomass. These components—including hemicellulose, lignin, and extractives – contribute to the bulk of the raw material but are undesirable for pure cellulose extraction.[36,37] Further loss in weight was observed after bleaching due to the removal of the remaining impurities, which resulted in a whiter appearance of the fibers.[38] The biomass composition of the untreated and treated SMS fibers was analyzed using the Chesson–Datta method to quantify the relative amounts of lignocellulosic materials—cellulose, hemicellulose, and lignin—as well as other residual impurities remaining after pre-treatment. Fig. 3 shows the changes in the percentages of these components after the pre-treatment processes. Untreated SMS fibers derived from *P. ostreatus* contained 24.19% ± 0.46 cellulose. Previous studies on SMS from the same mushroom species reported cellulose contents ranging from approximately 29 to 37%.[14,15,18] These variations in the cellulose content are influenced by the differences in the initial substrate materials used and cultivation practices.[4] In addition to cellulose, the untreated SMS also contained 18.98% ± 0.35 hemicellulose, and 28.41% ± 0.47 lignin, which are comparable to the findings of Adi *et al.*, who reported similar levels of structural polysaccharides in SMS.[39]

After treatment with increasing NaOH concentrations, significant compositional changes were observed. Cellulose content increased progressively from 29.8% at 2% to 64.36% at 32% NaOH, indicating effective preservation of cellulose. This substantial increase in cellulose content recovery is accompanied by a pronounced reduction in hemicellulose content, from 18.46% at 2% to a minimum of 12.62% at 16% NaOH, with a slight increase to 14.54% at 32% NaOH, suggesting some variability in hemicellulose removal at higher alkali concentrations. Lignin content showed a notable reduction from 29.67% at 2% to approximately 13.26% and 14.3% at 16% and 32% NaOH, respectively, confirming effective delignification with stronger alkali treatments. Ash content similarly declined sharply from 9.15% at 2% NaOH to just above 1% at 16% and 32% NaOH, indicating effective removal of inorganic impurities. Extractives also decreased from 12.93% at 2% NaOH to 5.68% at 32% NaOH, further evidencing purification.

Although both 16% and 32% NaOH treatments effectively removed impurities, no significant difference in the final

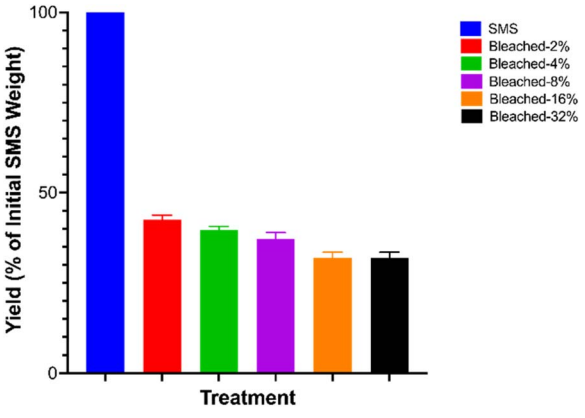

Fig. 2 Yield of cellulose nanofibers (CNF) obtained from spent mushroom substrate (SMS) following various chemical treatments, $n = 9$.

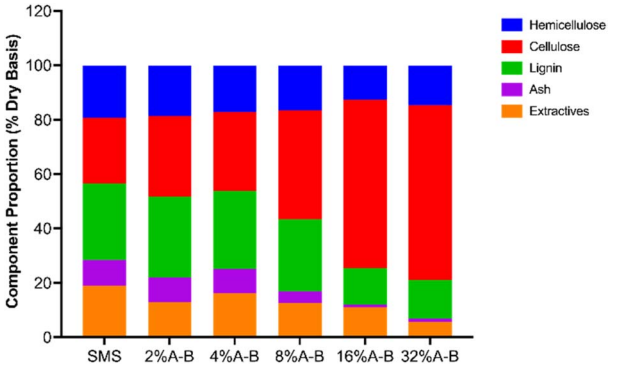

Fig. 3 Biomass composition (hemicellulose, cellulose, lignin, ash, and extractives) of untreated and chemically treated SMS fibers. Treatments include NaOH at varying concentrations (2%, 4%, 8%, 16%, and 32%) followed by bleaching, where A–B denotes alkali (NaOH) treatment followed by bleaching. Data are expressed as percentage of dry weight, $n = 9$.

cellulose content was detected between the two. Therefore, 16% NaOH-treated fibers were selected for the isolation of CNF, given their economic advantages, including lower chemical consumption and easier handling compared to the 32% NaOH-treated fibers. Additionally, the use of 16% NaOH-treated fibers offers a cost-effective and practical solution for large-scale production.

ATR-FTIR analysis of CNF

The extracted cellulose from the selected treatment was further subjected to TEMPO-mediated oxidation—a selective chemical modification process that converts the primary hydroxyl groups (–OH) on the cellulose chains into carboxylate groups (–COOH). This transformation enhances the surface charge of the fibers and improves their dispersibility in water, which is important for producing high-quality CNF. The oxidation process was confirmed using Attenuated Total Reflectance Fourier Transform Infrared (ATR-FTIR) to identify organic functional groups in the sample.

Fig. 4 presents the spectra of the SMS fibers after each treatment. The dominant spectral band observed around ~3350 corresponds to O–H stretching vibrations, while the peak ~1640 cm^{-1} is attributed to the C=O stretching of the carboxylate groups in the TEMPO-oxidized sample—indicating the successful conversion of the primary hydroxyl groups to carboxylates. Bands in the region of 1630–1650 cm^{-1} observed in the other samples represent the presence of adsorbed water, which is commonly retained within the cellulose matrix due to strong hydrogen bonding interactions and is difficult to eliminate completely.

Additional peaks at ~1370 cm^{-1} and ~1316 cm^{-1} correspond to C–H and O–H bending vibrations, respectively. The prominent band at ~1040 cm^{-1} is assigned to C–O–C stretching vibration in pyranose ring of cellulose, a hallmark of the cellulose backbone. Furthermore, the signal at 890–898 cm^{-1} is characteristic of cellulosic β-glycosidic bond stretching vibration in cellulose, confirming the preservation of the structural integrity of cellulose.

Overall, the ATR-FTIR analysis verified the successful oxidation of the cellulose, as indicated by the emergence of carboxylate-specific peaks while maintaining the key structural features of cellulose. These modifications improve the nanomaterial's functional properties—particularly water affinity and surface charge—making it better suited for applications requiring well-dispersed, high-performance CNF.[40,41]

Zeta potential, particle size distribution, and surface morphology of ToCNF

In addition to chemical oxidation, the fibers were subjected to mechanical disintegration to further reduce their diameter. Mechanical treatments, such as ultrasonication, are commonly employed to break down the cellulose fibers into nanofibers by applying shear forces that separate the fibers and reduce their size. This process is especially important in the production of CNF, as it significantly increase the surface area, improves dispersion, and enhances their mechanical strength and functional interactions with other composite systems.[42]

The resulting ToCNFs demonstrated a zeta potential ranging from 34.68 to −40.9 mV (Fig. 5), indicating a negatively charged surface area due to the introduction of the carboxylate groups during the oxidation process. A zeta potential of below −30 mV typically signifies strong electrostatic repulsion between the fibers, which is associated with good colloidal stability in aqueous suspensions.[43] This high surface charge helps prevent aggregation and ensures stable dispersion.[44]

SEM micrographs (Fig. 6) reveal that the ToCNFs possess high aspect ratio, with fiber diameters ranging from 42 nm to 216 nm. The nanofibers appeared web-like, overlapping bundles, making it challenging to determine their precise length due to the bundling and entanglement. This morphology is typical of cellulose nanofibers produced by TEMPO-mediated oxidation, consistent with the observations of Isogai and Zhou, who reported the overlapping, branched fibers with extended lengths in ToCNFs.[45] The observed network-like structure suggests that ToCNFs can form strong entanglements through hydrogen bonding, which is critical for reinforcing polymer matrices and improving mechanical properties in composite materials.[46,47] Fiber curling was also observed, a common morphological change during fibrillation and drying processes.[48] Similar curling phenomenon was reported by Wang *et al.*, who noted that this morphology can be hypothetically attributed to the residual starch and hemicellulose creating a physical barrier.[49] Levanič *et al.* likewise noted fiber curling and demonstrated that it can be minimized by fiber swelling

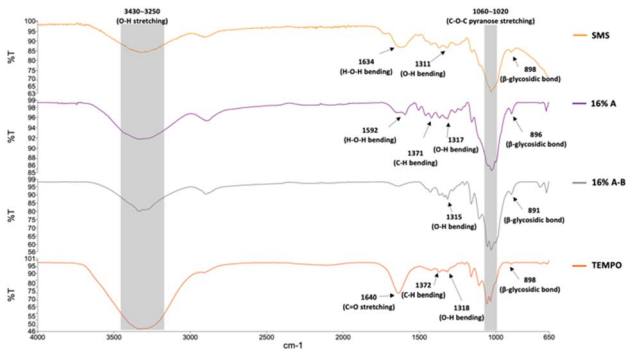

Fig. 4 ATR-FTIR spectra of untreated SMS, 16% A (16% NaOH-treated), 16% A–B (16% NaOH-treated followed by bleaching), and TEMPO (TEMPO-oxidized fibers).

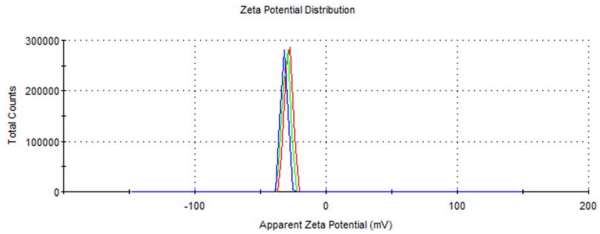

Fig. 5 Zeta potential distribution of TEMPO-oxidized cellulose nanofibers (ToCNF).

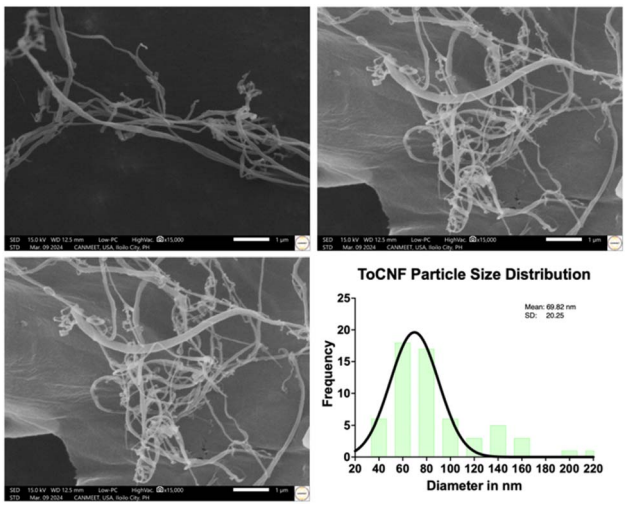

Fig. 6 SEM micrographs of ToCNFs taken at 15 000× magnification with a scale bar of 1 μm and the corresponding particle size distribution histogram illustrating the diameter range of the nanofibers, $n = 60$.

from prolonged TEMPO oxidation time and thorough pulp washing.[41] In this study, the observed curling may be further attributed to the lyophilization step, which commonly induces fiber shrinkage and aggregation due to the removal of bound water and structural collapse during freeze-drying.[50]

Simultaneous green synthesis and *in situ* loading of AgNPs to ToCNFs

Fig. 7 illustrates the synthesis route for the fabrication of AgNP/ToCNF. The process began with ion exchange between silver ions (Ag^+) and sodium ions (Na^+) present on the sodium salt form of the oxidized nanofibers, converting them into Ag^+-ToCNFs complex. This ion exchange reaction was conducted at 37 °C for 1 hour. During the thermal treatment, the fiber color changed from white to brown, indicating successful silver ion incorporation. Thereafter, the *in situ* reduction of the Ag^+ to AgNPs was carried out using WESMS.

In a previous study, WESMS was analyzed by LC-MS to identify its phytochemical constituents.[30] The presence of vanillic acid and decanoic acid derivatives in WESMS has been reported to act as reducing agents for producing AgNPs and

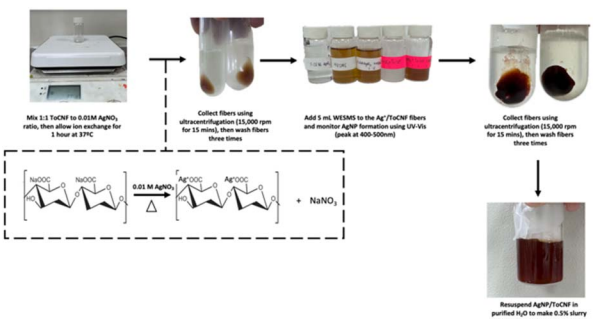

Fig. 7 Pictorial diagram of the simultaneous green synthesis and *in situ* loading of AgNPs onto ToCNFs.

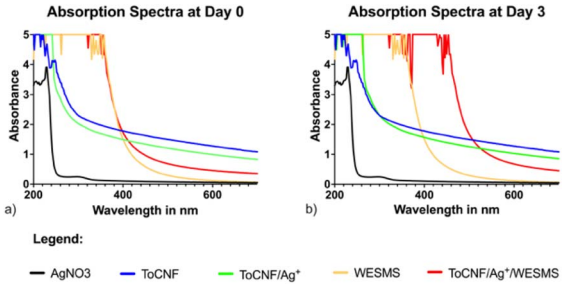

Fig. 8 UV-vis absorption spectra of AgNO3, ToCNFs, ToCNFs/Ag+, WESMS, ToCNFs/Ag+/WESMS on Day 0 (a) and Day 3 (b).

other metal nanoparticles.[31,32] The mixture was monitored daily using UV-vis spectroscopy to track the formation of AgNPs. A characteristic absorption peak between 400 and 500 nm indicates the successful reduction to AgNPs, attributable to the surface plasmon resonance of the AgNPs, which corresponds to the observed reddish-brown color change.[51] Fig. 8 presents the UV-vis spectra of Day 0 and Day 3 of the mixtures. On Day 3, the ToCNFs/Ag^+ sample showed no distinct absorption peak in the 400–500 nm range, whereas the ToCNFs/Ag^+/WESMS mixture exhibited clear absorption peaks within this range, confirming the role of WESMS as a reducing agent in the *in situ* synthesis of AgNPs on the ToCNFs. After thoroughly removing the unreacted reactants from the mixture by centrifugation at 15 000 rpm, AgNP/ToCNF was successfully isolated, with the maximum absorbance detected at 424 nm (Fig. 9). Additionally, the peaks observed at 200–230 nm corresponds to the characteristic absorption bands of CNF.

A similar reduction procedure was also performed on AgNPs without ToCNFs, and the reduction using WESMS was observed on Day 5, consistent with the findings of Suleman Ismail Abdalla *et al.*[30] This indicates that the presence of ToCNFs accelerates the nucleation and growth of AgNPs, likely due to the functional groups on the nanofiber surface acting as nucleation sites and stabilizers.[52] This synergistic effect between WESMS and ToCNFs not only facilitates faster reduction kinetics but also enables stable loading of AgNPs on the

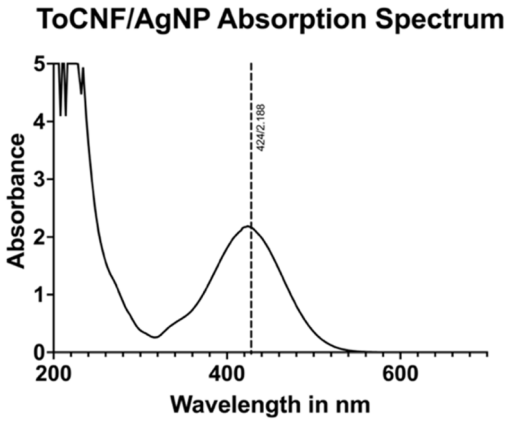

Fig. 9 UV-vis absorption spectrum of synthesized AgNP/ToCNF nanocomposite.

cellulose nanofiber matrix, which is advantageous for applications requiring well-dispersed metal nanoparticles with antimicrobial activity.

Zeta potential, particle size distribution, and surface morphology of AgNP/ToCNF

The zeta potential of the AgNP/ToCNF composite was −48.3 ± 0.58 mV, indicating good colloidal stability. SEM analysis revealed the size and surface morphology of the nanocomposite (Fig. 10). As shown in Fig. 10b, the mean diameter of reduced AgNPs loaded on the ToCNFs surface was 34.04 nm, while the ToCNFs exhibited a mean width diameter of 296 nm (Fig. 10d). The increase in the width diameter of ToCNFs compared to neat ToCNFs is attributed to the spherical AgNP deposition on the fiber surface. Similar morphological changes were observed by Smiechowicz *et al.*, where AgNP decoration led to increased fiber dimensions and enhanced surface roughness.[53]

This decoration of AgNPs resulted in a distinctly roughened nanocomposite surface (Fig. 10f) compared to the smooth surface observed on the neat ToCNFs (Fig. 10e), which is consistent with the findings of Jatoi *et al.*, who reported similar surface topography changes in AgNP-modified cellulose nanofibers.[54] Notably, the reduced AgNPs were well dispersed without significant agglomeration—an improvement over typical AgNP synthesis processes, where nanoparticle agglomeration is a common challenge.[55,56] This selective loading is likely due to the preferential attachment of silver nanoparticles to the oxidized regions of the cellulose structure, as previously reported.[57]

While the current study demonstrates the successful synthesis of AgNP/ToCNF nanocomposite, it is important to note that long-term stability assessments were beyond the scope of this work. Future studies should focus on evaluating the structural and functional stability of the materials under various storage and physiological conditions to further validate their practical applicability.

Evaluation of antibacterial activity

Preliminary screening for antibacterial activity of ToCNFs, AgNPs, and AgNP/ToCNF. The antibacterial activity of the test compounds was initially assessed using the agar well diffusion method. A zone of inhibition measuring 4.0 mm or greater was considered indicative of effective antibacterial activity. Fig. 11 shows the inhibition zones produced by the tested samples against the three bacterial strains, *S. aureus*, *E. coli*, and *P. aeruginosa*.

Ciprofloxacin (20 μg mL^{-1}) served as the positive control and exhibited the largest zones of inhibition, with mean diameters of 25.29 ± 1.19 mm, 27.85 ± 0.64 mm, and 15.02 ± 1.12 mm for *S. aureus*, *E. coli*, and *P. aeruginosa*, respectively (Table 1). As expected, ToCNF alone (both at 250 and 500 μg mL^{-1}) showed no antibacterial activity against any tested strain, consistent with previous findings by Jiang *et al.*[58]. In contrast, AgNPs demonstrated significant antibacterial effects at 500 μg mL^{-1}, producing large inhibition zones of 18.34 ± 1.47 mm, 20.61 ± 1.43 mm, and 13.38 ± 0.82 mm for *S. aureus*, *E. coli*, and *P. aeruginosa*, respectively. These values indicate strong antibacterial efficacy, approaching the activity of ciprofloxacin, especially against *P. aeruginosa*. The AgNP/ToCNF composite also exhibited antibacterial activity, though slightly reduced compared to AgNPs alone, with inhibition zones at 500 μg mL^{-1} measuring 13.17 ± 0.95 mm for *S. aureus*, 16.96 ± 0.40 mm for *E. coli*, and 11.23 ± 1.04 mm for *P. aeruginosa*. At the lower concentration of 250 μg mL^{-1}, both AgNPs and AgNP/ToCNF showed diminished antibacterial activity but maintained

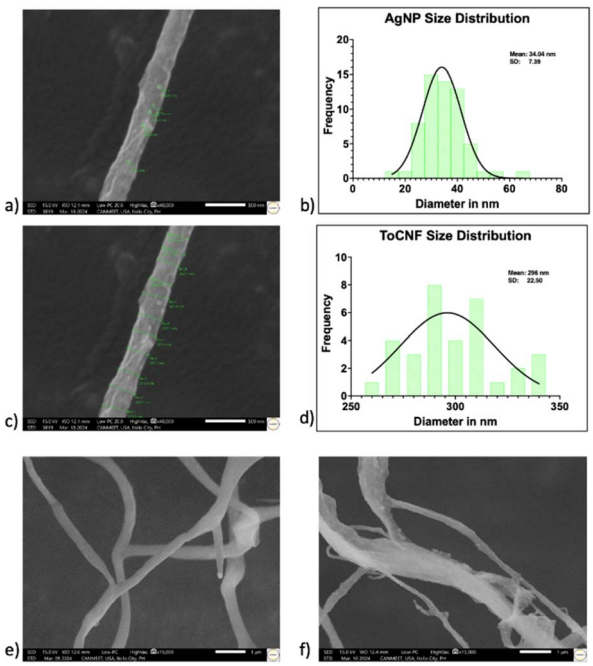

Fig. 10 SEM micrographs of (a) AgNPs at 40 000× magnification (scale bar = 500 nm) and their corresponding size distribution (b); (c) ToCNFs at 40 000× magnification (scale bar = 500 nm) with size distribution (d); and surface morphology comparison of (e) neat ToCNFs and (f) AgNP-loaded ToCNFs at 15 000× magnification (scale bar = 1 μm). Particle size distributions are based on n = 60 measurements.

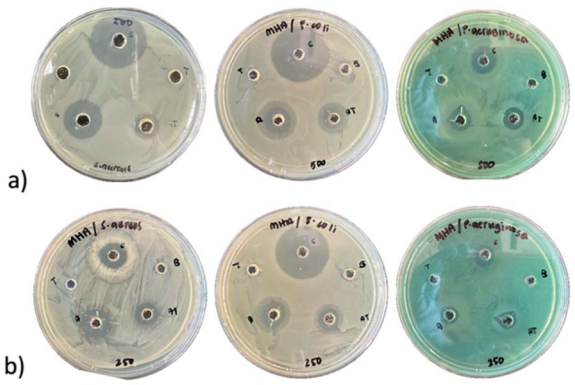

Fig. 11 Zones of inhibition of 500 μg mL^{-1} (a) and 250 μg mL^{-1} (b) of the different test compounds against *S. aureus* (left), *E. coli* (middle), and *P. aeruginosa* (right) grown on Mueller–Hinton agar. (Legend: C = ciprofloxacin, B = blank, T = ToCNF, A = AgNP, AT = AgNP/ToCNF).

Table 1 Zones of inhibition of ToCNF, AgNP, and AgNP/ToCNF against *S. aureus*, *E. coli*, and *P. aeruginosa*, $n = 6$[a]

	Inhibition zone diameter in mm		
	S. aureus	*E. coli*	*P. aeruginosa*
	Mean ± SD	Mean ± SD	Mean ± SD
Cipro20	25.29 ± 1.19	27.85 ± 0.64	15.02 ± 1.12
dH2O	—	—	—
T500	—	—	—
T250	—	—	—
A500	18.34 ± 1.47	20.61 ± 1.43	13.38 ± 0.82
A250	13.63 ± 1.32	15.87 ± 0.91	11.51 ± 0.87
AT500	13.17 ± 0.95	16.96 ± 0.40	11.23 ± 1.04
AT250	10.38 ± 0.68	11.62 ± 0.41	8.67 ± 1.21

[a] Abbreviations: Cipro20 = ciprofloxacin 20 μg mL^{-1}; T500 = ToCNF 500 μg mL^{-1}; A500 = AgNP 500 μg mL^{-1}; AT500 = AgNP/ToCNF 500 μg mL^{-1}.

measurable zones of inhibition. The lack of activity in ToCNFs alone confirms that the observed antibacterial effects are primarily attributable to the silver nanoparticles. These findings suggest that the incorporation of AgNPs into ToCNF effectively imparts antibacterial properties, making the composite a promising candidate for antimicrobial applications.

Minimum inhibitory concentration. The test compounds that exhibited antibacterial activity were further evaluated by the broth microdilution method to determine their MIC_{90}. AgNPs showed greater antibacterial activity against *E. coli*, with 97% inhibition at 31.25 μg mL^{-1} (Fig. 12d), while 93% inhibition was observed for *P. aeruginosa* at the same concentration (Fig. 12g). In comparison, *S. aureus* exhibited only 91% inhibition but at twice the concentration (Fig. 12a). A similar trend was observed for AgNP/ToCNF, where the MIC_{90} against *S. aureus* (250 μg mL^{-1}) (Fig. 12b) was twice that of the MIC_{90} against the Gram-negative bacterial strains (125 μg mL^{-1}) (Fig. 12e and h).

These findings align with previous studies demonstrating that Gram-negative bacteria are generally more susceptible to silver nanoparticles.[59–61] The exact mechanism of action of AgNPs remains an area of active research, but the most well-studied mechanism involves the ability of AgNPs to cause damage to bacterial cell membranes.[62,63] This is mainly due to their high surface area relative to volume; smaller particle sizes result in greater silver penetration into the cells, causing bacterial cell death. In our experiment, the higher concentration of both test compounds needed to achieve 90% growth inhibition against Gram-positive *S. aureus* compared to Gram-negative bacteria may be linked to differences in the structural composition of their cell walls. Cell walls of Gram-positive bacteria have a thicker peptidoglycan layer (~20–80 nm thick), whereas Gram-negative bacteria possess a much thinner peptidoglycan layer (~2–7 nm thick). The dense, multilayered peptidoglycan layer of Gram-positive bacteria acts as a protective barrier, reducing the diffusion of AgNPs into the cells.[64–66]

Another possible mechanism explaining the lower MIC of AgNP-containing compounds against Gram-negative bacteria is their ability to penetrate bacterial cells through porin channels in the outer membrane of Gram-negative bacteria. Porins are transmembrane proteins primarily involved in the passive transport of molecules of various sizes and charges across the membrane.[67] This provides an additional pathway for AgNP entry into Gram-negative bacterial cells, while Gram-positive bacteria rely solely on diffusion through their thick peptidoglycan layer—a much slower and less efficient process.

Additionally, the results showed that AgNPs were more potent across all bacterial strains compared to AgNP/ToCNF. This can be explained by the presence of ToCNFs: the *in situ* loading of AgNPs on ToCNFs limits the accessibility of the AgNPs to directly contact bacterial cells, which is crucial for their antibacterial activity while free AgNPs are more potent, their immobilization on ToCNF reduces their potency but serves an essential purpose—mitigating cytotoxicity while providing a slow release of AgNPs for a sustained antibacterial activity.[68] This trade-off is further discussed in the LDH cytotoxicity subsection.

Time-kill assay. The time-kill kinetics profiles offer valuable insight into the dynamics of antibacterial activity over time. As expected, bactericidal agents achieved a ≥3 log reduction in CFU mL^{-1} within 24 hours, while bacteriostatic agents resulted in less than a 3 log reduction. Ciprofloxacin (20 μg mL^{-1}) served as the positive control, demonstrating reliable antimicrobial efficacy, whereas untreated bacteria acted as the negative control.

For *S. aureus*, AgNPs exhibited bactericidal effects at concentrations of 62.5 μg mL^{-1} (MIC), 125 μg mL^{-1} (2× MIC), and 250 μg mL^{-1} (4× MIC), while AgNPs loaded on ToCNF required higher concentrations—250 μg mL^{-1} (MIC), 500 μg mL^{-1} (2× MIC), and 1000 μg mL^{-1} (4× MIC)—to achieve similar

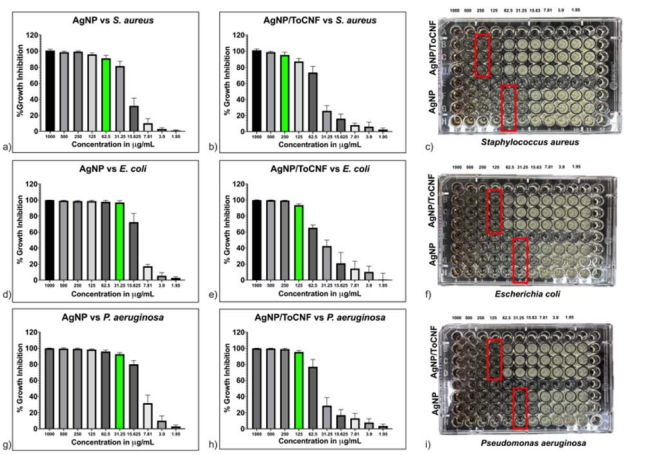

Fig. 12 MIC_{90} against *S. aureus* of AgNP (a) and AgNP/ToCNF (b) and photograph of the wells (c), against *E. coli* (d–f), and *P. aeruginosa* (gi); bar graphs data present the percentage of growth inhibition after 24 hours of treatment exposure measured by OD600. MIC_{90} against *S. aureus* of AgNP (a) and AgNP/ToCNF (b) and photograph of the wells (c), against *E. coli* (d–f), and *P. aeruginosa* (g–i); bar graphs data present the percentage of growth inhibition after 24 hours of treatment exposure measured by OD600. The experiment was done in triplicate and performed in three trials.

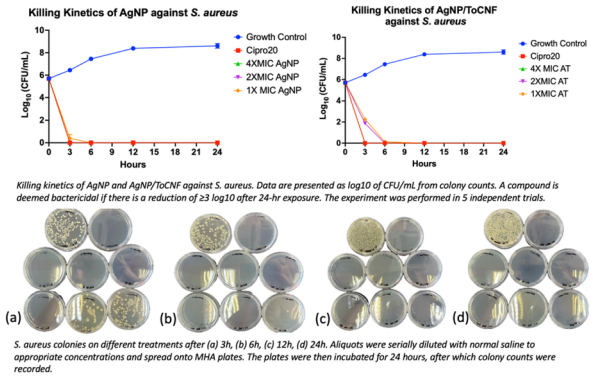

Fig. 13 Killing kinetics profile of AgNP and AgNP/ToCNF against *S. aureus* ($n = 5$). Representative culture plates of *S. aureus* are shown at (a) 3 h, (b) 6 h, (c) 12 h, and (d) 24 h following treatment.

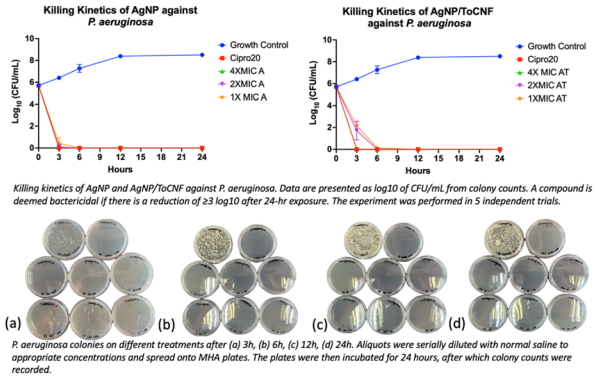

Fig. 15 Killing kinetics profile of AgNP and AgNP/ToCNF against *P. aeruginosa* ($n = 5$). Representative culture plates of *P. aeruginosa* are shown at (a) 3 h, (b) 6 h, (c) 12 h, and (d) 24 h following treatment.

effects. Conversely, for the Gram-negative bacteria *E. coli* and *P. aeruginosa*, both free AgNPs and AgNP/ToCNF demonstrated effective bactericidal activity at lower concentrations, reflecting the generally higher susceptibility of these strains.

The data depicted in Fig. 13–15 illustrate that both forms of AgNPs exerted potent bactericidal activity against all tested strains. Free AgNPs at 2× and 4× MIC rapidly reduced bacterial counts by 6 logs within just 3 hours, while the MIC concentration achieved the same reduction by 6 hours without any regrowth observed over the subsequent 24 hours. AgNP/ToCNF also demonstrated strong bactericidal properties, though with slightly delayed kinetics, reaching a 6 log reduction at 4× MIC within 3 hours and at lower concentrations by 6 hours. This concentration-dependent killing pattern underscores the sustained antimicrobial potential of both treatments. Importantly, the absence of bacterial regrowth during the 24-hour observation period, confirmed by an additional 24-hour incubation of culture plates, supports the conclusion that bacterial death rather than temporary inhibition was responsible for the observed effects.

Both test compounds were effective at eliminating 99.9999% bacterial populations. However, the more rapid and potent bactericidal action of free AgNPs compared to AgNP/ToCNF can be attributed to the greater immediate bioavailability and direct contact of silver nanoparticles with bacterial cells. Immobilization of AgNPs onto ToCNFs likely moderates their release, resulting in a slower but sustained antimicrobial effect.[34] This controlled release may offer advantages in reducing cytotoxicity and prolonging antibacterial efficacy, a trade-off that warrants consideration in therapeutic applications.

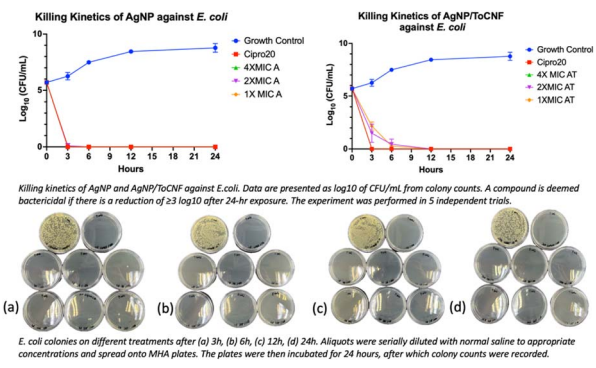

Fig. 14 Killing kinetics profile of AgNP and AgNP/ToCNF against *E. coli* ($n = 5$). Representative culture plates of *E. coli* are shown at (a) 3 h, (b) 6 h, (c) 12 h, and (d) 24 h following treatment.

Cell membrane leakage assay. The cell membrane leakage assay was performed to assess the integrity of bacterial cell membranes following exposure to the test compounds. Disruption of membrane integrity was evaluated by quantifying the leakage of intracellular components—specifically nucleic acids and proteins—into the extracellular medium. The presence of these biomolecules in the supernatant is a well-established indicator of membrane damage. Untreated bacterial cells were used as the negative control to establish baseline membrane integrity, while 5% Tween 80, a known membrane-permeabilizing agent, served as the positive control. The extent of membrane damage was expressed as a percentage of protein and nucleic acid leakage relative to the values observed with 5% Tween 80 treatment. Fig. 16 shows elevated absorbance

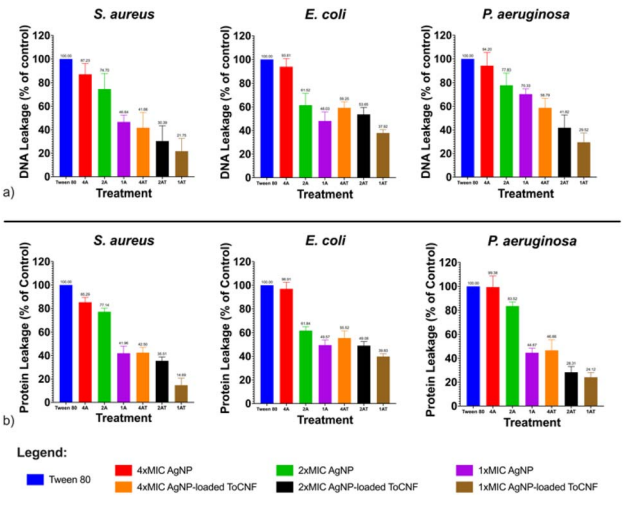

Fig. 16 Relative leakage of bacterial intracellular materials (a) DNA, at 260 nm; (b) proteins, at 280 nm for AgNPs and AgNP/ToCNF, $n = 9$.

at 260 nm and 280 nm following treatment with AgNP and AgNP/ToCNF, indicating the release of nucleic acids and proteins, respectively. These results suggest that both test compounds compromised bacterial cell membrane integrity. A concentration-dependent increase in leakage was observed, demonstrating a dose–responsive interaction between the AgNP-containing compounds and the bacterial membranes. Notably, the free-state AgNPs induced greater leakage of both DNA and proteins compared to AgNP/ToCNF, highlighting their more immediate and pronounced membrane-disruptive effect.

Moreover, the slightly lower levels of DNA and protein leakage observed in *S. aureus* compared to *E. coli* and *P. aeruginosa* further support the role of bacterial cell wall structure in modulating susceptibility to AgNP-based treatments. The thick, multilayered peptidoglycan wall of Gram-positive *S. aureus* likely acts as a barrier, limiting the penetration of AgNPs and reducing their subsequent interaction with the cytoplasmic membrane. In contrast, the thinner peptidoglycan layer and outer membrane of Gram-negative bacteria may facilitate easier access and internalization of AgNPs, resulting in greater membrane disruption and leakage.[65]

The cell membrane disruption induced by silver-containing compounds, particularly at the nanoscale, is closely associated with the particle size of AgNPs and their affinity for sulfur-containing proteins in the bacterial cell wall. Numerous studies have demonstrated that smaller AgNPs exhibit greater antibacterial activity, primarily due to their higher surface area-to-volume ratio, which enhances their interaction with bacterial membranes and intracellular targets.[69–72] This increased surface reactivity enables more effective attachment to the bacterial cell surface and facilitates penetration through the cell envelope.

Additionally, AgNPs are known to interact strongly with thiol (–SH) groups in sulfur-containing proteins present in the bacterial cell wall and membrane. This interaction leads to the denaturation of these proteins and irreversible structural alterations in the cell wall, ultimately compromising membrane integrity and function.[62,73] These combined properties—enhanced surface interaction due to small size and specific affinity for thiol groups—allow AgNPs to overcome bacterial defenses, disrupt the membrane, and induce cell lysis. Such mechanisms underpin the potent bactericidal activity observed in silver nanoparticles and their nanocomposites.

In vitro proliferative effects and cytotoxicity

The Alamar Blue assay was employed to assess the proliferative response of fibroblasts to AgNP and AgNP/ToCNF exposure. This assay measures cellular metabolic activity based on the reduction of resazurin, a non-fluorescent dye, to resorufin, a fluorescent and colorimetric compound. A decrease in resorufin signal indicates reduced metabolic activity, which corresponds to compromised cell viability or proliferation.[74,75] Fig. 17 illustrates the effects of the different treatments on fibroblast proliferation.

ToCNFs were tested for their proliferative effects on HDFs, showing little to no difference in cell proliferation compared to untreated controls. This biocompatibility aligns with previous findings.[76,77] Both untreated and ToCNF-treated cells exhibited high Alamar Blue (AB) reduction, indicating healthy metabolic activity and viability. In contrast, treatment with free-state AgNPs resulted in a dose- and time-dependent decrease in AB reduction, suggesting reduced metabolic activity at higher concentrations and longer exposure durations. A statistically significant reduction in metabolic activity was observed at concentrations of 125 μg mL^{-1} and above, likely due to cytotoxic effects. Time-course analysis further confirmed that prolonged exposure to AgNPs progressively decreased AB reduction. This decline in cell proliferation may be attributed to AgNP-induced

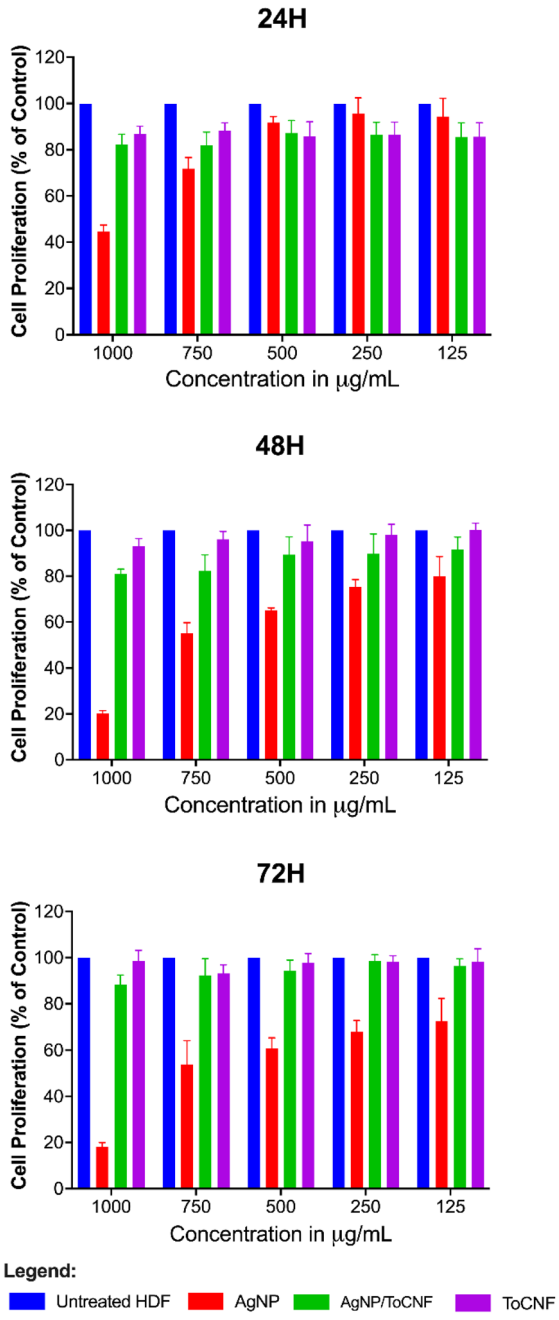

Fig. 17 Cell proliferation percentages at different time points relative to untreated cells for AgNP and AgNP/ToCNF ($n = 6$).

disruption of cellular metabolism, possibly *via* oxidative stress, mitochondrial damage, and depletion of intracellular antioxidants such as reduced glutathione.[78] Interestingly, the combination treatment (AgNP/ToCNF) did not significantly affect HDF metabolic activity or proliferation under the tested conditions, suggesting that the ToCNF matrix may mitigate the cytotoxic effects of AgNPs by moderating their release and limiting direct interaction with cells.

However, it is important to note that the Alamar Blue assay evaluates cell viability based on metabolic activity, which is an indirect indicator of cytotoxicity. To complement this, a lactate dehydrogenase (LDH) assay was performed to assess membrane integrity and quantify actual cell damage.

LDH is a stable cytoplasmic enzyme present in all cells and is released into the extracellular medium upon loss of membrane integrity. Its release serves as a hallmark of cellular damage due to apoptosis, necrosis, or other cytotoxic events. The LDH assay quantifies cell death by detecting NADH production during the conversion of lactate to pyruvate, which then reduces a tetrazolium salt (INT) into a red, water-soluble formazan product. The absorbance of formazan is directly proportional to the number of damaged or lysed cells.[79,80]

A concentration- and time-dependent increase in LDH release was observed in AgNP- and AgNP/ToCNF-treated cells, whereas ToCNFs induced only a slight, concentration-dependent increase in LDH release, with minimal variation across 72 hours (Fig. 18). Notably, AgNPs exhibited significant cytotoxicity at concentrations above 250 μg mL^{-1} after 24 hours of exposure, and marked LDH release was observed at concentrations of 125 μg mL^{-1} and higher from 48 to 72 hours. This trend suggests a cumulative cytotoxic effect, where extended exposure leads to progressive membrane damage.

In contrast, AgNP/ToCNF-treated cells showed no significant LDH release at concentrations up to 500 μg mL^{-1} across all time points, indicating reduced cytotoxicity. Furthermore, ToCNFs alone did not induce significant toxicity at any concentration tested, further supporting their biocompatibility.

As shown in Fig. 19, cells treated with free-state AgNPs exhibited noticeable deposition of nanoparticles on the cell surface, whereas this phenomenon was not observed in cells treated with AgNP/ToCNF. These findings suggest that the cytotoxic effects of free AgNPs are primarily mediated by disruption of cell membrane integrity, likely due to the accumulation of free silver particles on the cytoplasmic membrane. This accumulation may trigger a cascade of cellular responses, including oxidative stress, inflammatory signaling, DNA damage, lipid peroxidation, and ultimately, cell death *via* apoptosis and necrosis.[81–84] The significantly lower LDH release observed for AgNP/ToCNF across all concentrations and time points suggests that immobilizing AgNPs on the surface of ToCNFs reduces their bioavailability and limits direct interactions with the cell membrane. This indicates that the ToCNF carrier plays a modulating role by regulating the release of AgNPs, resulting in a slower, more controlled interaction with the membrane and thereby reducing cytotoxicity.[85] The demonstrated non-toxicity of ToCNFs reinforces their potential as a safe and biocompatible carrier for biomedical applications. This intrinsic biocompatibility likely plays a key role in mitigating the cytotoxic effects of the AgNP/ToCNF composite, contributing to its improved cellular compatibility compared to free-state AgNPs.

The precise mechanism governing the release of Ag^{+} ions from ToCNFs remains incompletely understood and warrants further investigation. Current hypotheses suggest that the release may occur through multiple pathways, including the desorption of loosely bound AgNPs from the nanofiber surface,

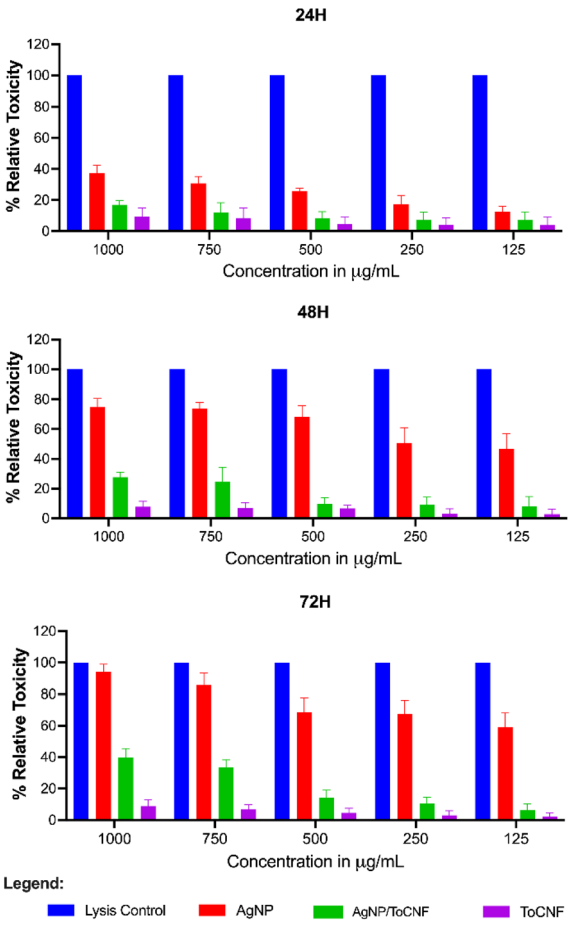

Fig. 18 Cytotoxicity of AgNP, AgNP/ToCNF, and ToCNFs relative to the lysis control ($n = 6$).

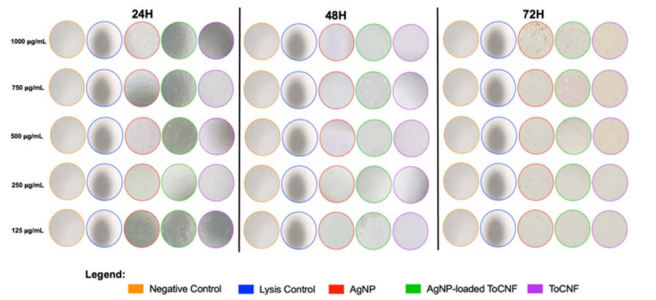

Fig. 19 Microscopic images of HDF captured under inverted microscope at 400× magnification at each time point of the LDH cytotoxicity assay.

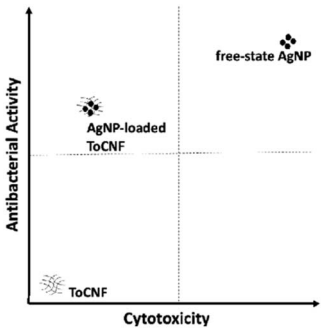

Fig. 20 Graphical representation of the relationship of antibacterial activity *vs.* cytotoxicity of ToCNF, AgNP, and AgNP/ToCNF.

the diffusion of Ag^+ ions from the nanofibers *via* oxidation of metallic silver (Ag^0) in the presence of oxygen and protons, and partial degradation and swelling of the ToCNF matrix.[60,86,87] These processes may collectively contribute to the gradual exposure and controlled release of silver from the composite material, but more detailed kinetic and mechanistic studies are needed, particularly under physiological conditions.

Fig. 20 illustrates the relationship between the antibacterial activity and cytotoxicity of the test compounds. While free-state AgNPs exhibit superior antibacterial efficacy compared to AgNP/ToCNF, their higher cytotoxicity restricts their suitability for biomedical applications. Conversely, AgNP/ToCNF shows slightly reduced antibacterial potency but significantly lower cytotoxicity relative to the free nanoparticles. The low cytotoxicity observed in AgNP/ToCNF, combined with its strong antibacterial activity—particularly at concentrations between 125 and 500 μg mL^{-1}—is likely due to the controlled release of AgNPs from the ToCNF matrix.

This controlled release mechanism enables effective penetration and disruption of bacterial membranes while minimizing harmful effects on mammalian cells. The differential susceptibility between bacterial and mammalian cells may be attributed to structural and functional differences; for instance, mammalian cells like HDF possess more robust repair and defense mechanisms that help mitigate damage from AgNP exposure.[88] However, further *in vivo* studies are necessary to validate these findings. Future research should focus on elucidating the precise release kinetics of AgNPs from the ToCNF matrix and assessing antibacterial efficacy and cytotoxicity within complex biological environments. Additionally, optimizing AgNP loading on the ToCNF scaffold could improve antibacterial performance while maintaining biocompatibility, thereby expanding its potential for diverse biomedical applications.

Conclusion

A green and sustainable method for synthesizing silver nanoparticles (AgNPs) *in situ* on TEMPO-oxidized cellulose nanofibers (ToCNFs) derived from spent mushroom (SMS), an underutilized agro-industrial residue, was successfully develop. The resulting AgNP/ToCNF nanocomposite exhibited potent, dose-dependent antibacterial activity (125–500 μg mL^{-1}) against both Gram-positive and Gram-negative bacterial strains, while demonstrating minimal cytotoxicity towards human dermal fibroblasts (HDFs).

Compared to free-state AgNPs, which showed rapid bactericidal effects but higher cytotoxicity, AgNP/ToCNF achieved comparable antibacterial efficacy with significantly reduced toxicity. This is attributed to the controlled release of silver ions from the ToCNF matrix, which limits direct nanoparticle–cell interaction, thus preserving mammalian cell viability. The observed membrane-disruptive mode of action and selective cytotoxicity underline the potential of the composite to selectively target microbial cells while sparing human cells. These findings highlight the potential of the nanocomposite synthesized from agricultural waste for biomedical applications, particularly in antimicrobial coatings and wound healing materials.

Future research should focus on evaluating the long-term stability and controlled release behavior of AgNP/ToCNF composites under physiological conditions. *In vivo* studies are essential to assess pharmacokinetics, biodistribution, efficacy, and biocompatibility. Scalability, reproducibility, cost-effectiveness, and environmental sustainability must also be addressed for clinical translation.

Additionally, integrating AgNP/ToCNF into formats such as wound dressings, implant coatings, medical textiles, and biodegradable packaging could enable eco-friendly antimicrobial solutions. Optimizing AgNP loading and release kinetics will be key to enhancing antibacterial efficacy while minimizing cytotoxicity across biomedical and environmental applications.

Data availability

The data presented in the study is available in the article.

Author contributions

Conceptualization, H. K.; methodology, C. M. K.; software, C. M. K.; validation, C. M. K.; formal analysis, C. M. K.; investigation, C. M. K.; resources, C. M. K.; data curation, C. M. K.; writing—original draft preparation, C. M. K.; writing—review and editing, H. K.; visualization, C. M. K.; supervision, H. K.; project administration, H. K.; funding acquisition, H. K.

Conflicts of interest

There are no conflicts to declare. The authors alone are responsible for the content and writing of this article.

Acknowledgements

The authors gratefully acknowledge the Faculty of Pharmacy, Universiti Kebangsaan Malaysia for their support in providing the materials necessary to conduct this research and the invaluable contributions made by the Department of Science and Technology-Science Education Institute (DOST-SEI) and

University of San Agustin. At the time of writing, C. M. K. was a recipient of the DOST-SEI scholarship.

Notes and references

1 B. Koul, M. Yakoob and M. P. Shah, *Environ. Res.*, 2022, **206**, 112285.
2 R. Phiri, S. Mavinkere Rangappa and S. Siengchin, *J. Cleaner Prod.*, 2024, **434**, 139989.
3 M. Duque-Acevedo, I. Lancellotti, F. Andreola, L. Barbieri, L. J. Belmonte-Ureña and F. Camacho-Ferre, *Environ. Sci. Eur.*, 2022, **34**, 70.
4 C. Martín, G. I. Zervakis, S. Xiong, G. Koutrotsios and K. O. Strætkvern, *Bioengineered*, 2023, **14**, 2252138.
5 A. Ravlikovsky, M. N. C. Pinheiro, L. Dinca, V. Crisan and L. Symochko, *Recycling*, 2024, **9**, 44.
6 K. N. Finney, C. Ryu, V. N. Sharifi and J. Swithenbank, *Bioresour. Technol.*, 2009, **100**, 310–315.
7 J. M. Marín-Benito, M. J. Sánchez-Martín and M. S. Rodríguez-Cruz, *Toxics*, 2016, **4**, 17.
8 J. Blair and S. Mataraarachchi, *Environments*, 2021, **8**, 73.
9 M. Dedousi, E.-M. Melanouri, D. Karayannis, E.-I. Kaminarides and P. Diamantopoulou, *Carbon Resour. Convers.*, 2024, **7**, 100196.
10 A. Siddiqua, J. N. Hahladakis and W. Al-Attiya, *Environ. Sci. Pollut. Res. Int.*, 2022, **29**, 58514–58536.
11 I. R. Abubakar, K. M. Maniruzzaman, U. L. Dano, F. S. AlShihri, M. S. AlShammari, S. M. S. Ahmed, W. A. G. Al-Gehlani and T. I. Alrawaf, *Int. J. Environ. Res. Public Health*, 2022, **19**, 12717.
12 R. Grover, A. Goel, L. Wati and K. Raj, *Pollut. Res.*, 2015, **34**, 121–124.
13 H. Li, S. Yoshida, N. Mitani, M. Egusa, M. Takagi, H. Izawa, T. Matsumoto, H. Kaminaka and S. Ifuku, *Carbohydr. Polym.*, 2022, **284**, 119233.
14 Z. Lou, Y. Sun, X. Zhou, S. A. Baig, B. Hu and X. Xu, *Geoderma*, 2017, **307**, 30–37.
15 S. J. Klausen, A. B. Falck-Ytter, K. O. Strætkvern and C. Martin, *Molecules*, 2023, **28**, 5140.
16 G. Koutrotsios, K. C. Mountzouris, I. Chatzipavlidis and G. I. Zervakis, *Food Chem.*, 2014, **161**, 127–135.
17 A. Shakir, B. Azahari, A. Salehabadi, Y. Yusup, M. Yhaya and M. Ahmad, *Int. J. Fluid Mech. Therm. Sci.*, 2020, **75**, 113–124.
18 G. Vasilakis, E. M. Rigos, N. Giannakis, P. Diamantopoulou and S. Papanikolaou, *Microorganisms*, 2023, **11**(2), 532.
19 S. Acharya, S. Liyanage, P. Parajuli, S. S. Rumi, J. L. Shamshina and N. Abidi, *Polymers*, 2021, **13**, 4344.
20 M. Madhushree, P. Vairavel, G. T. Mahesha and K. S. Bhat, *J. Nat. Fibers*, 2024, **21**, 2418357.
21 A. Suresh Khurd and B. Kandasubramanian, *Carbohydr. Polym. Technol. Appl.*, 2022, **4**, 100234.
22 J. Grondahl, K. Karisalmi and J. Vapaavuori, *Soft Matter*, 2021, **17**, 9842–9858.
23 P. Kaur, N. Sharma, M. Munagala, R. Rajkhowa, B. Aallardyce, Y. Shastri and R. Agrawal, *Front. Nanotechnol.*, 2021, **3**, 747329.
24 B. Thomas, M. C. Raj, A. K. B, R. M. H, J. Joy, A. Moores, G. L. Drisko and C. Sanchez, *Chem. Rev.*, 2018, **118**, 11575–11625.
25 S. Ventura-Cruz and A. Tecante, *Food Hydrocolloids*, 2021, **118**, 106771.
26 A. Zeng, B. Wang, M. N. Yiasmin, R. Yang, Y. Tong and W. Zhao, *Int. J. Biol. Macromol.*, 2024, **282**, 136897.
27 S. Rashki, N. Shakour, Z. Yousefi, M. Rezaei, M. Homayoonfal, E. Khabazian, F. Atyabi, F. Aslanbeigi, R. Safaei Lapavandani, S. Mazaheri, M. R. Hamblin and H. Mirzaei, *Front. Bioeng. Biotechnol.*, 2021, **9**, 732461.
28 A. Babaei-Ghazvini, R. Patel, B. Vafakish, A. F. A. Yazdi and B. Acharya, *Int. J. Biol. Macromol.*, 2024, **278**, 135200.
29 K. Patel, J. Shaikh and T. Khan, in *Handbook of Nanocelluloses: Classification, Properties, Fabrication, and Emerging Applications*, ed. A. Barhoum, Springer International Publishing, Cham, 2020, pp. 1–33, DOI: 10.1007/978-3-030-62976-2_42-1.
30 S. Suleman Ismail Abdalla, H. Katas, J. Y. Chan, P. Ganasan, F. Azmi and M. Fauzi Mh Busra, *RSC Adv.*, 2020, **10**, 4969–4983.
31 M. Scampicchio, J. Wang, A. J. Blasco, A. Sanchez Arribas, S. Mannino and A. Escarpa, *Anal. Chem.*, 2006, **78**, 2060–2063.
32 H. Zamani and A. Moradshahi, *Mol. Biol. Res. Commun.*, 2013, 47–55.
33 A. Isogai, T. Saito and H. Fukuzumi, *Nanoscale*, 2011, **3**, 71–85.
34 J. U. Shin, J. Gwon, S. Y. Lee and H. S. Yoo, *ACS Omega*, 2018, **3**, 16150–16157.
35 F. C. Tenover, L. M. Weigel, P. C. Appelbaum, L. K. McDougal, J. Chaitram, S. McAllister, N. Clark, G. Killgore, C. M. O'Hara, L. Jevitt, J. B. Patel and B. Bozdogan, *Antimicrob. Agents Chemother.*, 2004, **48**, 275–280.
36 O. Romruen, T. Karbowiak, W. Tongdeesoontorn, K. A. Shiekh and S. Rawdkuen, *Polymers*, 2022, **14**(9), 1830.
37 R. S. Abolore, S. Jaiswal and A. K. Jaiswal, *Carbohydr. Polym. Technol. Appl.*, 2024, **7**, 100396.
38 F. Hamzah, A. Idris and T. K. Shuan, *Biomass Bioenergy*, 2011, **35**, 1055–1059.
39 M. Adi, T. N. Tengku Izhar, N. Mohamad Ibrahim, N. Abd Aziz, H. Hadiyanto and M. Matei, *IOP Conf. Ser. Earth Environ. Sci.*, 2023, **1216**, 012015.
40 N. Huynh, J. J. Valle-Delgado, W. Fang, S. Arola and M. Österberg, *Carbohydr. Polym.*, 2023, **317**, 121095.
41 J. Levanič, V. P. Šenk, P. Nadrah, I. Poljanšek, P. Oven and A. Haapala, *ACS Sustain. Chem. Eng.*, 2020, **8**, 17752–17762.
42 O. Nechyporchuk, M. N. Belgacem and J. Bras, *Ind. Crops Prod.*, 2016, **93**, 2–25.
43 G. Lowry, R. Hill, S. Harper, A. Rawle, C. Hendren, F. Klaessig, U. Nobbmann, P. Sayre and J. Rumble, *Environ. Sci.: Nano*, 2016, **3**, 953–965.
44 G. Chinga-Carrasco, E. Pasquier, A. Solberg, I. Leirset, J. S. Stevanic, J. Rosendahl and J. Håkansson, *Carbohydr. Polym.*, 2023, **314**, 120923.

45 A. Isogai and Y. Zhou, *Curr. Opin. Solid State Mater. Sci.*, 2019, **23**, 101–106.
46 I. Besbes, S. Alila and S. Boufi, *Carbohydr. Polym.*, 2011, **84**, 975–983.
47 X. Xu, F. Liu, L. Jiang, J. Y. Zhu, D. Haagenson and D. P. Wiesenborn, *ACS Appl. Mater. Interfaces*, 2013, **5**, 2999–3009.
48 E. Afra, H. Yousefi, M. M. Hadilam and T. Nishino, *Carbohydr. Polym.*, 2013, **97**, 725–730.
49 Y. Wang, T. Pääkkönen, L. Solhi, N. Yousefi and E. Kontturi, *Carbohydr. Polym.*, 2025, **354**, 123315.
50 T. M. Oyinloye and W. B. Yoon, *Processes*, 2020, **8**, 354.
51 M. Sastry, K. Mayya and K. Bandyopadhyay, *Colloids Surf., A*, 1997, **127**, 221–228.
52 K. Nabeela, R. T. Thomas, J. B. Nair, K. K. Maiti, K. G. K. Warrier and S. Pillai, *ACS Appl. Mater. Interfaces*, 2016, **8**, 29242–29251.
53 E. Smiechowicz, B. Niekraszewicz and P. Kulpinski, *Materials*, 2021, **14**, 4126.
54 A. W. Jatoi, I. S. Kim and Q. Q. Ni, *Mater. Sci. Eng., C*, 2019, **98**, 1179–1195.
55 L. Wei, J. Lu, H. Xu, A. Patel, Z. S. Chen and G. Chen, *Drug Discovery Today*, 2015, **20**, 595–601.
56 Z. Mat Lazim, S. Salmiati, M. Marpongahtun, N. Z. Arman, M. R. Mohd Haniffah, S. Azman, E. L. Yong and M. R. Salim, *Water*, 2023, **15**, 1349.
57 H. Ito, M. Sakata, C. Hongo, T. Matsumoto and T. Nishino, *Nanocomposites*, 2018, **4**, 167–177.
58 N. Jiang, Y. Hu and Y. Cheng, *Polymers*, 2024, **16**, 1016.
59 E. D. Cavassin, L. F. P. de Figueiredo, J. P. Otoch, M. M. Seckler, R. A. de Oliveira, F. F. Franco, V. S. Marangoni, V. Zucolotto, A. S. S. Levin and S. F. Costa, *J. Nanobiotechnol.*, 2015, **13**, 64.
60 D. Dechojarassri, K. Komatsu, A. Sawara, H. Tamura and T. Furuike, *Fibers*, 2023, **11**, 69.
61 A. S. Dove, D. I. Dzurny, W. R. Dees, N. Qin, C. C. Nunez Rodriguez, L. A. Alt, G. L. Ellward, J. A. Best, N. G. Rudawski, K. Fujii and D. M. Czyż, *Front. Microbiol.*, 2023, **13**, 1064095.
62 T. C. Dakal, A. Kumar, R. S. Majumdar and V. Yadav, *Front. Microbiol.*, 2016, **7**, 1831.
63 E. O. Mikhailova, *Antibiotics*, 2025, **14**, 5.
64 S. Anees Ahmad, S. Sachi Das, A. Khatoon, M. Tahir Ansari, M. Afzal, M. Saquib Hasnain and A. Kumar Nayak, *Mater. Sci. Energy Technol.*, 2020, **3**, 756–769.
65 P. R. More, S. Pandit, A. D. Filippis, G. Franci, I. Mijakovic and M. Galdiero, *Microorganisms*, 2023, **11**, 369.
66 I. X. Yin, J. Zhang, I. S. Zhao, M. L. Mei, Q. Li and C. H. Chu, *Int. J. Nanomed.*, 2020, **15**, 2555–2562.
67 E. O. Mikhailova, *J. Funct. Biomater.*, 2020, **11**, 84.
68 S. Elayaraja, K. Zagorsek, F. Li and J. Xiang, *Carbohydr. Polym.*, 2017, **166**, 329–337.
69 S. Pal, Y. K. Tak and J. M. Song, *Appl. Environ. Microbiol.*, 2007, **73**, 1712–1720.
70 L. F. Espinosa-Cristóbal, G. A. Martínez-Castañón, R. E. Martínez-Martínez, J. P. Loyola-Rodríguez, N. Patiño-Marín, J. F. Reyes-Macías and F. Ruiz, *Mater. Lett.*, 2009, **63**, 2603–2606.
71 S.-H. Kim, H.-S. Lee, D.-S. Ryu and S.-J. Choi, *Microbiol. Biotechnol. Lett.*, 2011, **39**, 77–85.
72 J. Li, K. Rong, H. Zhao, F. Li, Z. Lu and R. Chen, *J. Nanosci. Nanotechnol.*, 2013, **13**, 6806–6813.
73 T. Bruna, F. Maldonado-Bravo, P. Jara and N. Caro, *Int. J. Mol. Sci.*, 2021, **22**, 7202.
74 M. N. Dinh, M. Hitomi, Z. A. Al-Turaihi and J. G. Scott, *MethodsX*, 2024, **13**, 103024.
75 E. M. Longhin, N. El Yamani, E. Rundén-Pran and M. Dusinska, *Front. Toxicol.*, 2022, **4**, 981701.
76 H. He, X. Shi, W. Chen, R. Chen, C. Zhao and S. Wang, *J. Agric. Food Chem.*, 2020, **68**, 7425–7433.
77 R. Kummala, D. Soto Véliz, Z. Fang, W. Xu, T. Abitbol, C. Xu and M. Toivakka, *Biomacromolecules*, 2020, **21**, 1560–1567.
78 M. J. Piao, K. A. Kang, I. K. Lee, H. S. Kim, S. Kim, J. Y. Choi, J. Choi and J. W. Hyun, *Toxicol. Lett.*, 2011, **201**, 92–100.
79 P. Kumar, A. Nagarajan and P. D. Uchil, *Cold Spring Harb. Protoc.*, 2018, 2018.
80 T. Riss, A. Niles, R. Moravec, N. Karassina and J. Vidugiriene, *Cytotoxicity Assays: in Vitro Methods to Measure Dead Cells, Eli Lilly & Company and the National Center for Advancing Translational Sciences, Bethesda (MD)*, 2004.
81 N. S. Alharbi and A. I. Felimban, *J. King Saud Univ., Sci.*, 2023, **35**, 102972.
82 S. Arora, J. Jain, J. M. Rajwade and K. M. Paknikar, *Toxicol. Lett.*, 2008, **179**, 93–100.
83 M. M. Rohde, C. M. Snyder, J. Sloop, S. R. Solst, G. L. Donati, D. R. Spitz, C. M. Furdui and R. Singh, *Part. Fibre Toxicol.*, 2021, **18**, 37.
84 T. Zhang, L. Wang, Q. Chen and C. Chen, *Yonsei Med. J.*, 2014, **55**, 283–291.
85 J. Wu, Y. Zheng, W. Song, J. Luan, X. Wen, Z. Wu, X. Chen, Q. Wang and S. Guo, *Carbohydr. Polym.*, 2014, **102**, 762–771.
86 G. Sabarees, V. Velmurugan, G. P. Tamilarasi, V. Alagarsamy and V. Raja Solomon, *Polymers*, 2022, **14**, 3994.
87 Z. Adamczyk, M. Oćwieja, H. Mrowiec, S. Walas and D. Lupa, *J. Colloid Interface Sci.*, 2016, **469**, 355–364.
88 Y. Lu, G. Pan, Z. Wei, Y. Li and X. Pan, *Exp. Gerontol.*, 2024, **196**, 112559.